Earth and Planetary Science Letters 426 (2015) 143–153

Contents lists available at ScienceDirect

Earth and Planetary Science Letters

www.elsevier.com/locate/epsl

Seismic evidence for a chemically distinct thermochemical reservoir in Earth's deep mantle beneath Hawaii

Chunpeng Zhao [a], Edward J. Garnero [a,*], Allen K. McNamara [a], Nicholas Schmerr [b], Richard W. Carlson [c]

[a] School of Earth and Space Exploration, Arizona State University, Tempe, AZ 85287-6004, USA
[b] Department of Geology, University of Maryland, College Park, MD 20742, USA
[c] Department of Terrestrial Magnetism, Carnegie Institution of Washington, 5241 Broad Branch Road, NW, Washington, DC 20015-1305, USA

A R T I C L E I N F O

Article history:
Received 12 November 2014
Received in revised form 2 June 2015
Accepted 5 June 2015
Available online 3 July 2015
Editor: P. Shearer

Keywords:
seismology
body wave
mantle structure
thermochemical pile
mantle convection
mantle plume

A B S T R A C T

Nearly antipodal continent-sized zones of reduced seismic shear wave velocities exist at the base of Earth's mantle, one beneath the Pacific Ocean, the other beneath the South Atlantic Ocean and Africa. Geophysicists have attributed the low velocity zones to elevated temperatures associated with large-scale mantle convection processes, specifically, hot mantle upwelling in response to cooler subduction-related downwelling currents. Hypotheses have included superplumes, isochemical heterogeneity, and stable as well as metastable basal thermochemical piles. Here we analyze waveform broadening and travel times of S waves from 11 deep focus earthquakes in the southwest Pacific recorded in North America, resulting in 8500 seismograms studied that sample the deep mantle beneath the Pacific. Waveform broadening is referenced to a mean S-wave shape constructed for each event, to define a relative "misfit". Large misfits are consistent with multipathing that can broaden wave pulses. Misfits of deep mantle sampling S-waves infer that the structure in the northeast part of the low velocity province beneath the Pacific has a sharp side as well as a sloping sharp top to the feature. This sharp boundary morphology is consistent with geodynamic predictions for a stable thermochemical reservoir. The peak of the imaged pile is below Hawaii, supporting the hypothesis of a whole mantle plume beneath the hotspot.

1. Introduction

The present-day chemistry and dynamics of Earth's deep mantle relate to how the mantle as a whole operates, today as well as in the past, including processes relating to the formation and evolution of the planet's core. The behavior of the deep mantle also may influence a number of surface phenomena ranging from driving large-volume intraplate volcanism to regulating the frequency of magnetic reversals. Data that help to constrain our understanding of the deep interior span the geo-disciplines, but seismology provides the most direct means of imaging deep structural features across a range of spatial scales.

Seismic tomography has revealed the presence of two nearly antipodal large low shear velocity provinces (LLSVPs) at the base of the mantle (Masters et al., 2000; Mégnin and Romanowicz, 2000; Grand, 2002; Houser et al., 2008; Ritsema et al., 2011; Lekic et al., 2012). These LLSVPs are located beneath Africa and the Pacific, regions that exhibit numerous surface hotspots and are far removed from deep extensions of current and geologically recent subduction (Fig. 1a). An apparent anti- or non-correlation between bulk and shear modulus in some LLSVP regions (Masters et al., 2000) along with suggestion of increased density (Ishii and Tromp, 1999; Trampert et al., 2004) support the possibility that they may be compositionally-distinct from the background lower mantle.

The strongest horizontal gradients in tomographically derived shear velocity occur at the LLSVP margins (e.g., Thorne et al., 2004; Torsvik et al., 2010; Lekic et al., 2012), which coincide with sharp transitions (50–100 km or less) found in high-resolution seismic studies (Ritsema et al., 1998; Wen, 2001; Luo et al., 2001; Ni et al., 2002; Ford et al., 2006; To et al., 2005; Sun et al., 2007; He and Wen, 2009, 2012) (Fig. 1b, Fig. S1, Supplementary Material). The high-resolution analyses primarily rely upon pulse-broadening of seismic waves that traverse the lowest 100–200 km of the mantle (Fig. S2, see also Table S1, Supplementary Material). This pulse-broadening occurs when seismic energy travels both outside and inside the LLSVP, often resulting in two distinct arrivals.

The vertical extent of LLSVP structure up off the core–mantle boundary (CMB), including sharp edges, has also been inferred by seismic wave travel times in several studies (Ritsema et al., 1998;

* Corresponding author.
E-mail address: garnero@asu.edu (E.J. Garnero).

http://dx.doi.org/10.1016/j.epsl.2015.06.012

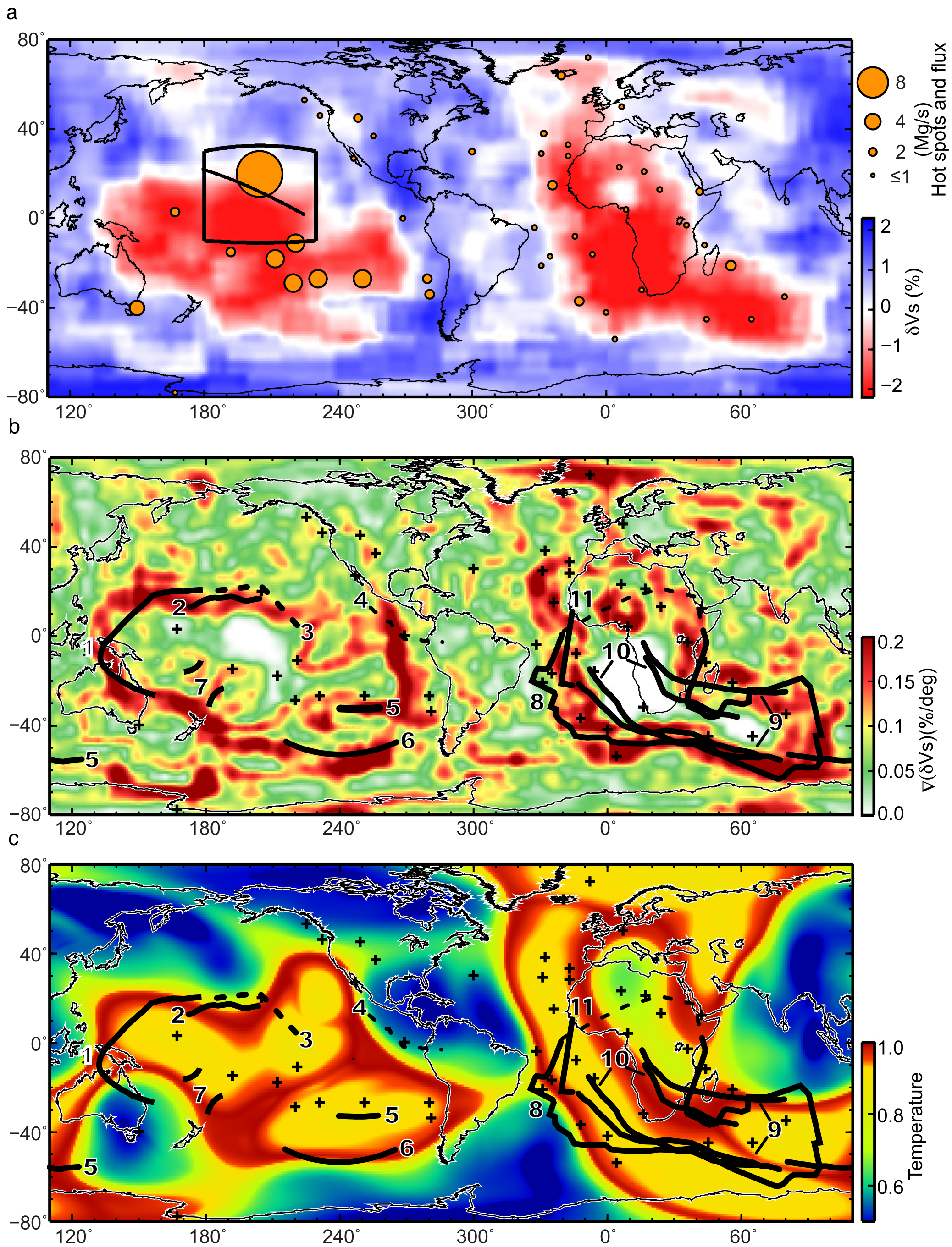

Fig. 1. Geographic correlation between lowermost mantle shear velocity tomography, lateral gradients, and imaged edges. (a) Hotspot locations (orange circles) are plotted on top of a global tomography shear velocity model TXBW (Grand, 2002) at 2750 km depth. Blue and red colors represent higher and lower velocities, respectively. Hotspot size is scaled to the flux of each hotspot (Sleep, 1990). The black box denotes the study region of this paper. The solid black line inside of the box indicates the location of the cross-section in Fig. 6. (b) Lateral shear velocity gradients in model TXBW (red = strongest gradients) are plotted with LLSVP edges (thick black lines, dashed if from travel time inference) found in previous studies (numbers in the figure correspond to Table S1, prominently). Hotspot locations are crosses. Gradients are calculated following a least-square linear curve-fitting algorithm (Thorne et al., 2004). (c) Similar to (b), but displayed are lateral variations of the temperature field calculated from a thermochemical convection model (Garnero and McNamara, 2008). Strongest gradients in (b) and temperatures in (c) are similar – they are near LLSVP margins found in high-resolution studies.

Wen, 2001; He and Wen, 2009, 2012; Lekic et al., 2012). Some of these studies fix the shear velocity reduction within the LLSVP to be a constant value, resulting in a trade-off between velocity reduction and imaged LLSVP height (and shape). Thus, while the geographical distribution of reduced shear velocities in the lowest couple hundred km appears fairly well established (e.g., Becker and Boschi, 2002; Lekic et al., 2012), LLSVP structure up into the lower mantle is less so.

The height and morphology of LLSVP structure depends critically upon the density and viscosity differences between the LLSVP and the surrounding mantle (McNamara and Zhong, 2005; Tackley et al., 2005; Tan et al., 2011). Several possible dynamical frameworks are presented in Fig. 2. Each of the four possibilities in Fig. 2 holds promise in matching the two principle seismic observations of significant shear velocity reductions in the LLSVP and sharp LLSVP sides. However, different geometries

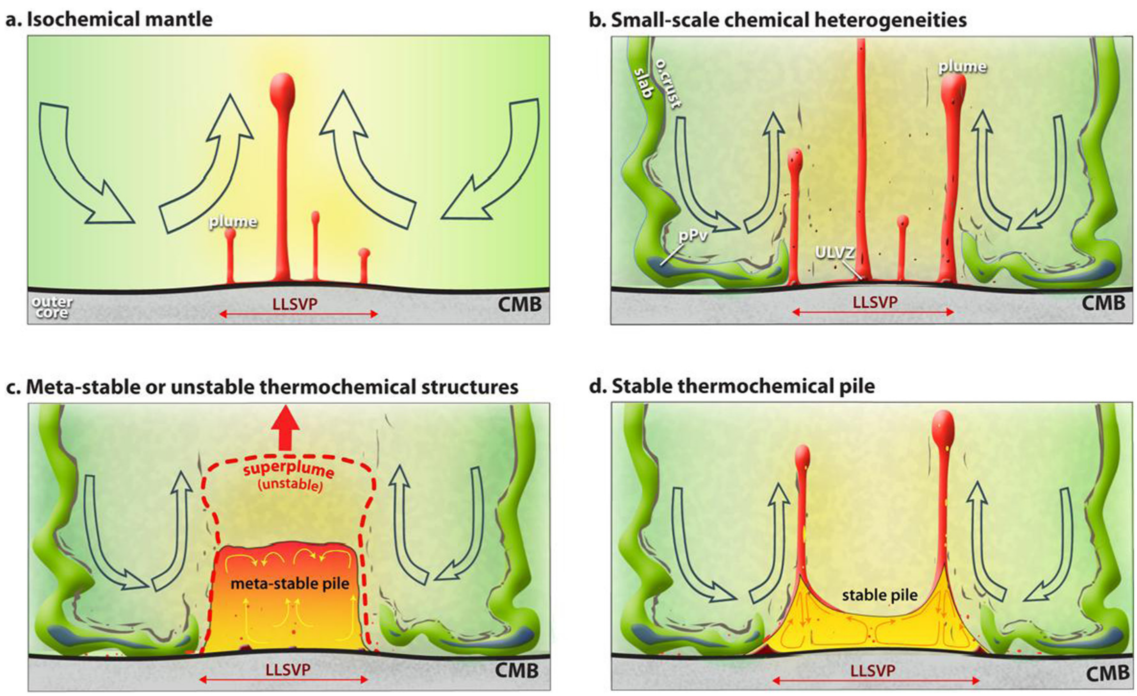

Fig. 2. Scenarios that can result in an LLSVP. (a) In an isochemical mantle, upwelling and plumes can be concentrated in areas away from beneath downwelling, and the warmer upwelling zone can be an LLSVP, though the sides may not be uniformly sharp. (b) Former lithosphere and oceanic crust, as well as ultra-low velocity zone (ULVZ) material can introduce small-scale heterogeneities into the lowermost mantle, and enhance the seismically imaged contrast between the LLSVP and surrounding mantle. (c) A nearly neutrally buoyant thermochemical structure can have vertical sides and a shape that depends strongly on internal properties (called a meta-stable pile). If unstable, the whole structure may break away from the CMB as a superplume (red dashed line). (d) With density slightly elevated, the thermochemical pile becomes a stable structure with sloped sides and plumes coming off ridges. For both (c) and (d), small-scale heterogeneities can mix into the thermochemical material. In all cases, the zone labeled LLSVP will be beneath upwelling, away from cold downwelling zones. (For interpretation of the references to color in this figure legend, the reader is referred to the web version of this article.)

are predicted for the slope of the LLSVP sides and the LLSVP top, which warrants some brief discussion on their dynamical aspects. For example, in a purely isochemical mantle, large-scale convection patterns are expected to focus mantle plumes (perhaps into plume clusters) within larger-scale upwelling regions (Fig. 2a) (e.g., Schubert et al., 2004, 2009; McNamara and Zhong, 2005; Bull et al., 2009; Davies et al., 2012). However, subducted oceanic lithosphere (Christensen and Hofmann, 1994; Brandenburg and van Keken, 2007), ultra-low velocity zone (ULVZ) material (Rost and Earle, 2010), and reaction products between the mantle and core (Manga and Jeanloz, 1996) are expected to introduce small-scale heterogeneity into the upwelling, plume regions (Fig. 2b).

A critical question relates to the stability of these structures. If the LLSVPs have a low enough density contrast with the surrounding background mantle, the resulting structures will become unstable and either become convectively entrained or form oscillating thermochemical superplumes that undergo episodes of rising within the mantle, cooling, and then descending back into the lower mantle (Davaille, 1999) (Fig. 2c). For higher density contrasts, the resulting structures are expected to remain stable and long-lived (Tackley, 2002, 2012; McNamara and Zhong, 2004). The morphology of long-lived stable structures is expected to be ridge-like, namely sloped sides that terminate at a cusp at the top, where plumes form (Fig. 2d). Alternatively, Tan and Gurnis (2005) demonstrate the formation of "metastable" structures with vertical sides that are more box-shaped, caused by the LLSVPs having a different bulk modulus from the surrounding mantle (Fig. 2c). Stable or metastable piles might possess a seismically detectable top. In contrast, isochemical plume clusters should have low seismic wave speeds that extend upwards, lacking an abrupt top to the velocity reductions. The scenarios depicted in Fig. 2 also differ from each other in several other aspects, including: heat flow from the core, capacity to sequester and provide the compositionally distinct source materials of ocean island basalts (OIBs) compared to mid-ocean ridge basalts (MORBs), and the nature and distribution of small scale heterogeneity.

In this study, we measure the S waveform broadening and travel times in a systematic attempt to study the shape of the northwestern portion of the Pacific LLSVP that underlies the Hawaiian hotspot (Fig. 1). In the sections that follow we map the depth and velocity reduction of the LLSVP top in a focused region by matching time and waveform broadening measurements between 1D models and data.

2. Seismic dataset

We analyze seismic data that densely sample the northeastern part of the Pacific LLSVP beneath Hawaii. Past studies of LLSVP edges (Table S1, Supplementary Material, Fig. 1) focused on the lowermost 100–200 km of the mantle. Here we explore LLSVP margins further up off the CMB by analyzing S-wave data with turning depths throughout the lowest 1000 km of the mantle (within and above the tomographically imaged LLSVP). For the shallower parts of this depth range, epicentral distances between 75 and 85 degrees provide the best coverage. Earthquakes in the southwest Pacific recorded by seismic stations on the west coast of North America enable investigation of the Pacific LLSVP beneath Hawaii at this distance range; much of our data was obtained from USArray stations deployed as part of the EarthScope project (http://earthscope.org). These USArray stations permit sampling the deep mantle beneath Hawaii with unprecedented wave path density. Stations in the central and eastern United States have wave paths that bottom in the lowermost 100–200 km of the mantle, thus, while we include those, we focus more on the western US stations (Fig. S3, Supplementary Material). Our dataset consists of 8500 seismograms from 11 intermediate- to deep-focus (>120 km) Fiji–Tonga earthquakes (Table S2, Supplementary Material).

3. Data processing method

Waveform broadening was quantitatively determined for all S-waves in this dataset. We developed an iterative stacking algorithm to define an empirical source wavelet shape for each earthquake, effectively a mean S-wave shape for each earthquake that simultaneously documents wave shape and travel time anomalies for individual records of each event. This objectively identified broadened waveform pulse-widths relative to the empirical source wavelet, and provided a "misfit" estimate that characterized the difference between the wave shape of each S-wave and that of the empirical wavelet. We defined the waveform "misfit" measurement in terms of a percentage of a waveform's deviation from the mean shape of S-waves on an event-by-event basis. Relatively narrow or broadened records have negative or positive misfit values, respectively. Misfits and travel time perturbations relative to a reference model were determined by the following steps:

(1) *Empirical source wavelet construction*. For each event, a time window from 15 s before and 30 s after direct S on the transverse component of motion was defined, using predictions from the PREM model (Dziewonski and Anderson, 1981). The maximum amplitude in this time window was normalized to unity. On displacement recordings, these 45 s long time windows were linearly summed to make an initial stack. Records with S-waves close in time to ScS were omitted. The initial stack was iteratively updated by the following procedure: (a) each record was aligned with the initial stack using cross-correlation, and polarity-checked and corrected if necessary; (b) its shift time and cross-correlation coefficient (CCC_Z) was stored; (c) using the CCC_Z's as weights, records were re-summed to make a new stack, omitting any record with $CCC_Z < 0.5$; this empirical cut-off value was chosen based on visual inspection of records, records below this value were typically noisy. This iterative procedure, sometimes referred to as adaptive stacking (Rawlinson and Kennett, 2004), was continued until the updated stack wave shape was nearly identical with the previous stack, as defined by the CCC_Z between a previous and updated stack being greater than 0.999. We defined this final stack as the empirical source stack (ESS) for this event. As part of this first step, all discarded ($CCC_Z < 0.5$) and retained records were visually inspected to insure the automation procedure was operating properly.

(2) *Definition of empirical source timing onset*. The ESS was used to estimate the timing of individual records (relative to predictions made with the PREM model). We employed an algorithm to objectively and automatically define the relative onset timing of the ESS pulse. First, a noise level was defined as the maximum amplitude in a 5 s long time window, starting 14 s before the S-wave peak in the ESS. S-wave onsets were typically smooth in the ESS's. Therefore, we used the time derivative of the displacement recording ESS, which sharpens the commencement of the S-wave pulse. The onset was then defined as the time value where the amplitude of the ESS pulse (in velocity) exceeds the pre-determined noise level value. The velocity ESS pulse grows out of the background noise more quickly than displacement; this, combined with the background energy being very low in the ESS stacks, resulted in (a) an onset time for the ESS in displacement that agrees with where we would pick it by hand, but (b) the automated process being more objective and uniform (thus robust), albeit, while empirical.

(3) *Computation of individual waveform misfit and timing*. For each event, all retained S-waves were cross-correlated with the ESS. They were then windowed from the ESS onset time to an end time defined by 2.5 times the peak-minus-onset time. This added 50% more time window after the S-wave peak than the onset-to-peak time, which we chose based on inspection of the data, which showed steeper ramp up to the peak than decay from the peak (in displacement recordings). The aligned and normalized record and

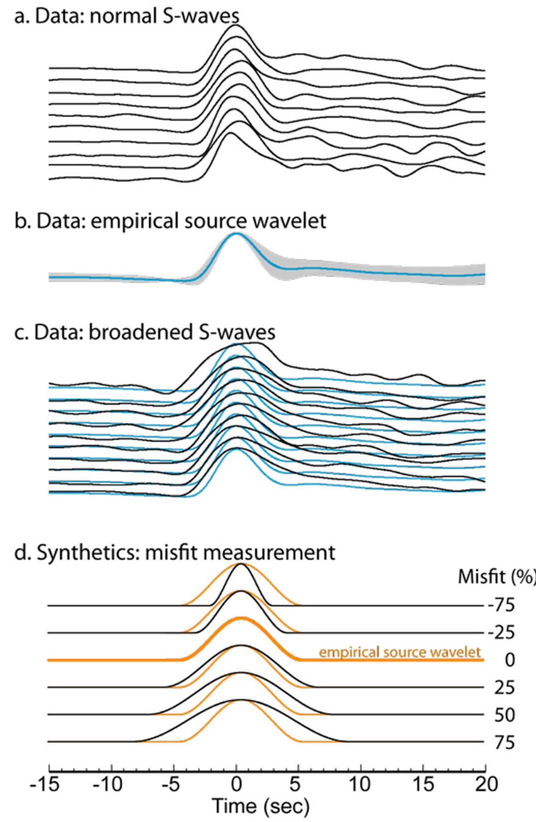

Fig. 3. Waveform examples of misfit measurements. For the earthquake of August 26, 2007, we show (a) ten "normal" waveforms of the S-wave, defined by having a misfit value ∼0%, and thus closely resemble the empirical source shape shown in (b) (thick black line); gray shading displays the standard deviation of this stack. (c) Similar to (a), except ten broadened waveforms are shown (thin black lines), defined by large misfit values (∼40%). Thin gray line traces are the empirical source from (b). (d) This synthetic example demonstrates the relationship between waveform broadening and misfit value (computed as described in the Data processing and method section in the main text) for a simple sinusoid stretched by different amounts. The record with zero % misfit is defined as the empirical source, and is repeated as the gray trace for the non-zero misfit records (which are black). Thus a 100% misfit record is roughly twice as wide as the empirical source shape; a 50% misfit value corresponds to a record roughly $\frac{1}{2}$ as wide as the empirical source shape.

ESS were subtracted; the result was integrated, and then divided by the integrated ESS. We thus defined a misfit as the relative difference between the area beneath each record's wave shape and that of the ESS stack for the specified time window, in percent:

$$Misfit = \frac{S^i_{rec} - S_{ESS}}{S_{ESS}} \times 100\%$$

S^i_{rec} represents the area under the curve of the ith record, and S_{ESS} denotes the area under the curve of the ESS stack. Thus, records narrower or broader than the ESS would have negative or positive misfit values, respectively. Records that were broadened due to wave multi-pathing (Ni et al., 2002; To et al., 2005; Ford et al., 2006) may have contributed to erroneously broadening the ESS, i.e., resulting in an ESS that does not simply represent the earthquake's source time function. We circumvented this outcome by re-computing Step 2 solely with records containing negative misfit values, resulting in a new empirical source stack, denoted ESS′. ESS′ represents the narrowest half of the waveshape population. This population is referred to as the "normal" waveforms (e.g., Fig. 3). Waveform misfit for each record was then re-computed, as defined above, except using ESS′. This process also re-computed the timing anomaly of each S-wave onset via cross-correlating each record with ESS′.

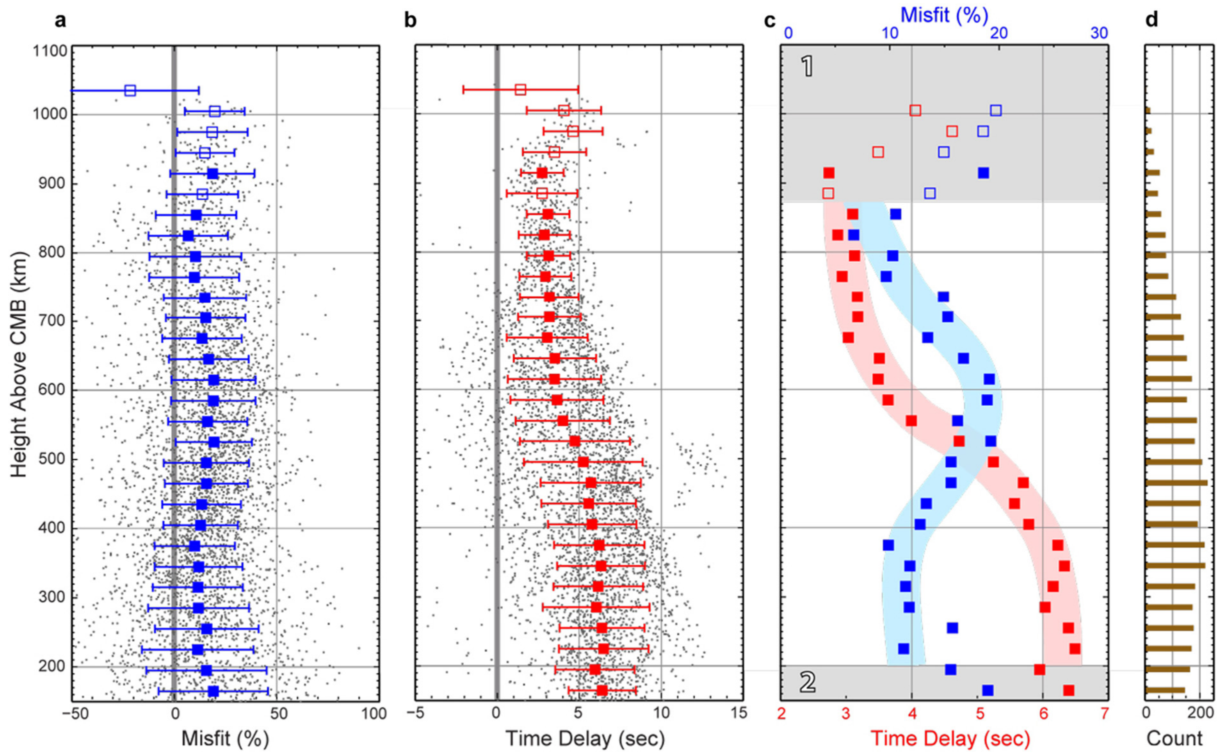

Fig. 4. Waveform misfits and travel time delays for the entire dataset. S-wave waveform misfits and time delays are shown for our entire data set as a function of PREM-predicted wave bottoming depth above the CMB. Individual misfit measurements (a) and travel time delay measurements (b) are gray dots, and are accompanied with mean values in 30 km depth intervals with ± one standard deviation (horizontal bars). Open squares correspond to 30 km depth intervals with less than 50 data points. Panel (c) compares the mean values from (a) and (b) with slightly expanded horizontal scales. For most of the robustly sampled depth bins, the maximum misfits and travel time delays appear to occur at different depths (near 600 km above the CMB for the misfits, and in the lower 400 km of the mantle for the travel time delays). We omit focus on the two gray regions: region 1 corresponds to too few data, region 2 corresponds to complications in the misfit measurement due to contamination by ScS. (d) Number of records within each 30 km bin.

Travel times of individual records are computed in velocity traces, to emphasize the first half of the displacement trace, by cross correlating with the velocity version of the ESS. This helped to minimize possible errors from convolving a broad observed waveform with a narrow ESS. All correlations used for travel times were subsequently visually inspected to insure that the correlation scheme worked (poor correlation-based times were discarded).

These choices in windowing and stacking parameters were developed by extensive trial and error tests to achieve the most stable mean shape of each event, i.e., ESS', as well as onset times and misfit measurements across different earthquakes with different source time functions. While subjective, this procedure is consistent across events in how it documents relative waveform broadening and travel time anomalies (Fig. 3).

After discarding records with poor signal quality, our final dataset retained more than 4700 high quality seismograms that densely sample a 30 × 40 degree area in the lowermost 1000 km of the mantle beneath the northeastern Pacific (Fig. S3, Supplementary Material).

4. Results

Fig. 3 presents an example of normal versus broadened waveforms for an earthquake in our dataset, and demonstrates the concept of our misfit measurement. A more complete set of waveforms, misfits, and travel times for this event are shown in Fig. S4 (Supplementary Material). Waveform misfits and travel time delays for our entire dataset are summarized in Fig. 4. Several features are apparent: (1) significant scatter is present, consistent with the levels of heterogeneity previously identified beneath the central Pacific (Tan and Gurnis, 2005); (2) waveform misfits on average are greatest some 600 km above the CMB (Fig. 4c); and (3) travel time delays are greatest in the lowest 400 km of the mantle. These data enable investigation of LLSVP structure beneath Hawaii further up from the CMB than previously possible.

If LLSVPs have a distinct top due to compositional heterogeneity, there can be an associated seismic waveform effect. We consider a pronounced LLSVP structure to emphasize these possible effects; an 800 km thick LLSVP (Fig. 5a) is introduced (and we note this may be unrealistically large). A seismic wave at 80 degrees epicentral distance will have an additional arrival that reflects from the underside of the LLSVP top (Fig. 5b); this additional wave arrives after the direct S wave and broadens the S pulse, and is apparent in the misfit measurements (Fig. 5c and 5d). Thus the top of an LLSVP, if possessing contrasting seismic properties, may be detectable from the additional underside reflected S-waves broadening the direct S-wave pulse. The misfit and travel time predictions in Fig. 5d are not dissimilar from the averaged measurements of our data set sampling below Hawaii (Fig. 4c): the misfit distribution has a peak at a depth below which the travel time delays begin increasing. However, we note that this idealized form of a large LLSVP is a low velocity zone that bends wave paths deeper – thus the details of any particular model will determine the degree to which refraction (or diffraction) in the mantle just above (as well as below) the LLSVP top will play an important role in the wavefield; this includes the possibility of a shadow zone from the low velocity LLSVP. For this reason, computation of synthetic seismograms is important for modeling observations.

The azimuthal span of our data (Fig. S3, Supplementary Material) permits us to investigate variations in the Pacific LLSVP in the NW-to-SE direction (Fig. 1a, Fig. S5, Supplementary Material). Spatial patterns in waveform misfits are clearly present

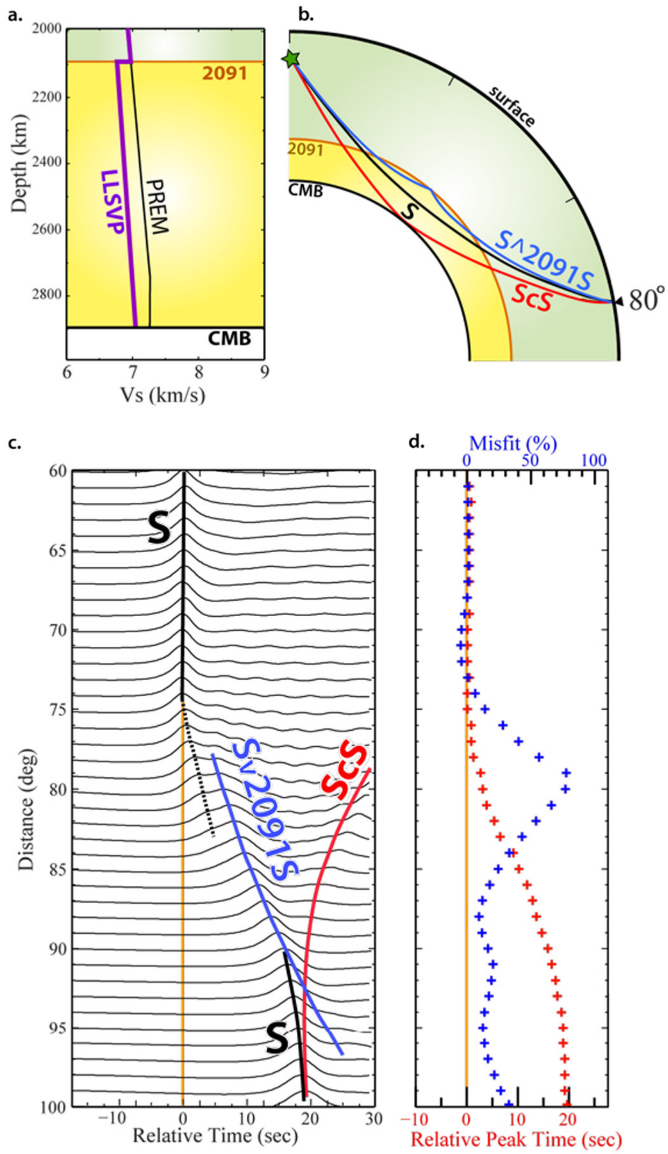

Fig. 5. Synthetics for a lower mantle possessing an LLSVP. (a) Shear velocity-depth profile showing an 800 km thick LLSVP. (b) Ray paths of seismic waves that contribute to the broadening of a deep mantle S-wave: the core reflected ScS and the wave that reflects from the underside of the top of the LLSVP, here, dubbed Sˆ2091S, for an epicentral distance of 80 degrees. Waves that diffract or refract along the LLSVP top may also contribute, depending on the model and distance. (c) Reflectivity method (Müller, 1985) displacement synthetic seismograms for the tangential component. Traces are plotted relative to that predicted by the PREM model (Dziewonski and Anderson, 1981). At around 77 degrees the S-wave becomes multi-pulsed due to the Sˆ2091S arrival, thus becoming broadened. The wave group is delayed at larger distances due to the reduced shear wave velocities of the LLSVP. (d) The misfit (blue) and travel time delays (red) are shown for measurements on the synthetic seismograms of panel (c). As with the observations (Fig. 4), the misfits have a peak several 100 km above the CMB from the LLSVP top, and travel time delays increase for deeper diving waves. (For interpretation of the references to color in this figure legend, the reader is referred to the web version of this article.)

(Fig. 6a), which, to the first order, outline the upper edge of the LLSVP imaged in tomography (Fig. 6a). Large misfits along the well-sampled NW and SE edges trend diagonally up the LLSVP and connect at a depth of about 600 km above the CMB, which appears to correspond to the top of the tomographically derived LLSVP. While this consistency depends to some extent on the tomographic model chosen for comparison, all the S-wave tomography models have LLSVPs (e.g., see Becker and Boschi, 2002; Lekic et al., 2012), thus there is a transition from LLSVP velocities to "normal" overlying mantle at some point. Our misfits are also overlain on our S-wave travel time delays (Fig. 6d). Our travel time delays (thus, plausibly low LLSVP velocities) extend further up into the lower mantle than the tomography model in Fig. 6b. This shape of the misfit distribution in Fig. 6 cross-sections compares well with the temperature field from a 3-D numerical convection model (Fig. 6c) with a dense basal compositionally-distinct reservoir (Garnero and McNamara, 2008), where an initially uniform dense basal layer is assumed (255 km thick; thicker or thinner layers result in larger or smaller piles, respectively), with 119 Ma of plate motions imposed at the surface. Misfit patterns cannot be due to the earthquake source or receiver regions because events are distributed up and down the Fiji–Tonga trench, whereas misfits have geometric consistencies with their spatial distribution of waveform broadening near their bottoming depths. However, S-waves bottoming in the lowest 200 km of the mantle are close in time to the core-reflected ScS (Fig. 5c), which can result in erroneously large misfits for distances beyond 95 degrees. Furthermore, the presence of a strong velocity change at the LLSVP top produces an additional arrival that propagates just above the LLSVP, at first as a refraction and then as a diffraction, which further contaminates the misfit measurement of waves bottoming in the lowest 200 km of the mantle (Fig. S6, Supplementary Material). Possible sources to the misfit from the upper mantle are discussed later in the Discussion section.

5. Modeling

For a narrow azimuthal portion of the cross-section (shaded region, Fig. 6a), the depth distribution of the misfit averages (Fig. 6e) and time delay averages (Fig. 6f) were simultaneously modeled by a least square fit to predictions from our 1D model database (Fig. S7, Supplementary Material). The lowest 200 km of the mantle is excluded in the depth profiles of Fig. 6e–g, since the large misfits in the deepest mantle likely contain contributions from the presence of ScS, as well as SvDS ($D =$ depth of LLSVP top, e.g., Fig. 5), possible refractions along the top of the LLSVP, and possibly high attenuation (discussed later). We computed synthetic seismograms for more than 1000 one-dimensional (1-D) models using the reflectivity method (Müller, 1985). We varied three principle features associated with a lowermost mantle low velocity region: (a) the velocity reduction magnitude, from 0 to -3.5%, in 0.5% intervals; (b) the sharpness of the transition from "normal" (PREM) overlying mantle to the LLSVP, from 0 to 350 km for the thickness of the gradient zone, in 50 km intervals; and (c) LLSVP thickness, in 50 km increments, defined as the distance from the CMB to the base of the gradient zone (or the discontinuity, if the gradient is zero). Waveform misfits and delay times are shown in Fig. S7 (Supplementary Material) for synthetics measured exactly the same way as the data. They show significant effects depending on the structural details of the LLSVP structure. Larger LLSVP shear velocity reductions yield larger waveform misfits and delay times (Fig. S7a, Supplementary Material). A 20% increase in the maximum waveform misfit can be caused by only 0.5% added velocity reduction in the LLSVP. The depth of the peak in the waveform misfit plot depends strongly on LLSVP velocity reduction, but is generally close to that of the discontinuity at the top of the LLSVP. The velocity gradient on top of the LLSVP affects the misfit amplitude and depth range over which the waveform misfit variations occur (Fig. S7b, Supplementary Material). Thicker velocity gradients result in weaker misfit values, and broadened distribution of misfit values near the depth of the LLSVP top. For a fixed LLSVP velocity reduction and gradient width at the LLSVP top, Fig. S7c (Supplementary Material) shows the dependency of the misfits and travel times on the LLSVP thickness. Fig. 5 shows the synthetic waveforms, measured misfit and

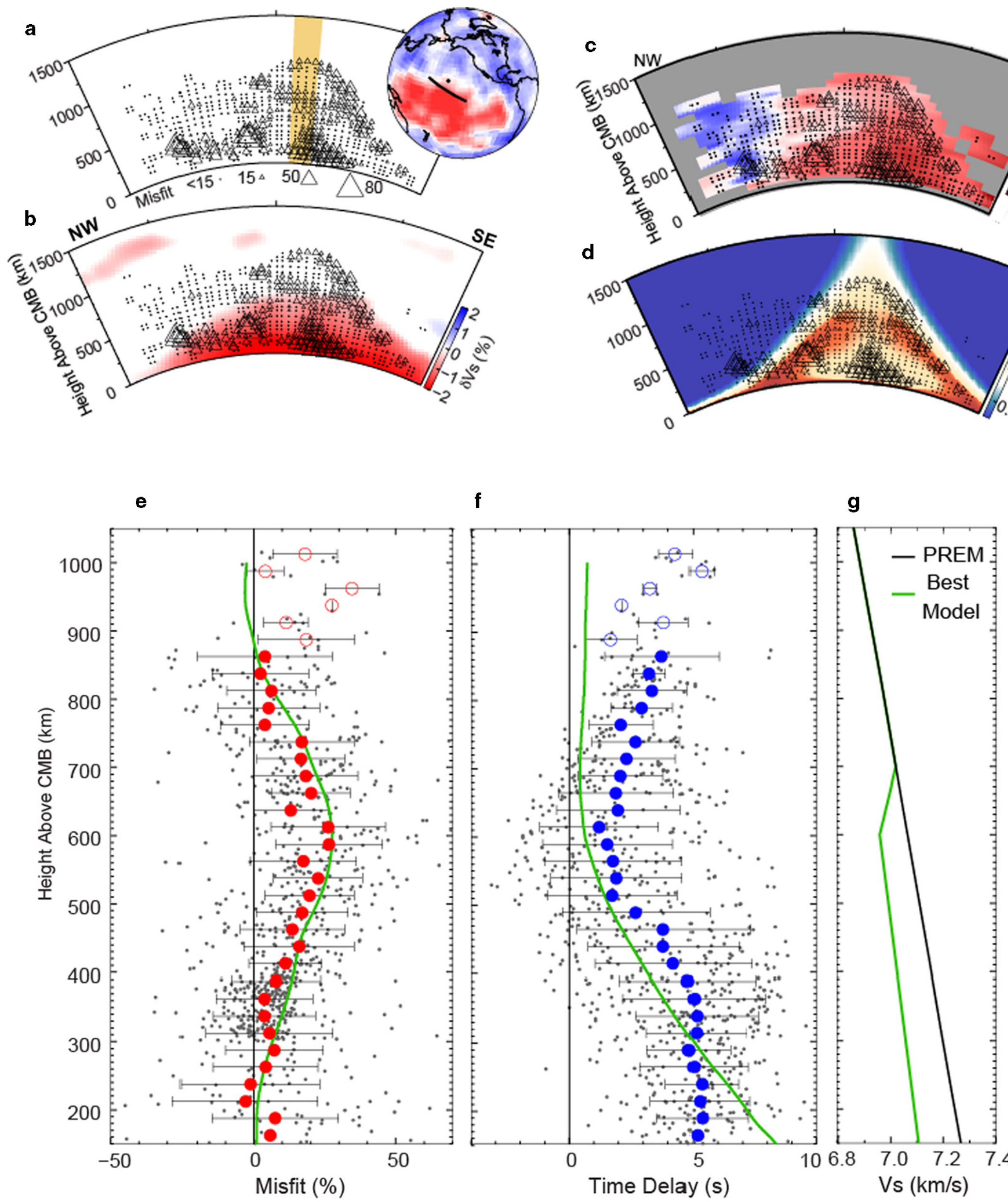

Fig. 6. Waveform misfits cross-section maps and modeling results. (a) A 50-degree wide cross-section (location indicated in Fig. 1a), with misfit values (triangles) projected to cross-section, overlying tomography model TXBW (Grand, 2002). Tan shaded box highlights azimuth range of the data plotted in (d) and (e). (b) As in (a), plotted on top of shear velocity reductions of a mantle tomography model (Grand, 2002). (c) As in (a), but misfits are plotted on top of our measured travel time anomalies, which have been smoothed (reds and blues correspond to delayed and advanced times, respectively). (d) As in (a), plotted on top of a temperature snapshot of a numerical flow model (Garnero and McNamara, 2008), which has a chemically distinct dense pile at the base of the mantle. Misfit values from (a) are plotted on top, and demonstrate the consistency between our observations with the reservoir hypothesis. (e) Misfits (gray dots) and 30 km wide depth-bin averages (red circles, with ±1 standard deviation) are plotted with respect to the S wave bottoming depth. Open circles represent depth-bins with less than 10 records. Solid red line is a prediction for our best-fitting 1-D reservoir model shown in (g). (f) As in (e) except travel time anomalies are shown (gray dots) with depth-bin averages (blue circles). Solid blue line is the prediction for our best-fitting model shown in (g). (g) Shear velocity versus depth of our best-fitting 1-D reservoir model (red) compared to PREM (black) for data in the shaded azimuth window in panel (a).

travel times for one such model. The details of the misfit measurements are shown to also depend on interfering phases (e.g., ScS).

In a grid search fashion, we established a measure of goodness of fit of each 1-D model to the observations as follows. (a) We computed the cross-correlation coefficient between the depth distribution of predicted and observed misfits (CCC_Z); for the observations, we used the depth-bin averages for the correlation. This established the degree to which the shapes of the depth distributions agree. (b) We accounted for the amplitude of the misfit versus depth variation by comparing the peak misfit amplitude of synthetics and observations, and combining with the CCC_Z for a measure of goodness of fit:

$$Goodness\_of\_fit = CCC_z \times \left(1 - \frac{A_s - A_d}{A_d}\right)^2$$

where A_s is the peak misfit amplitude in synthetics and A_d is the peak misfit amplitude in the data averages.

Misfit and travel time anomalies measured from synthetics depend strongly on basic LLSVP properties, while misfit amplitude depends strongly upon the strength of LLSVP velocity reduction. The sharpness of the top of the LLSVP affects the epicentral distance range (and hence wave bottoming depth) in which the misfit is maximum. LLSVP overall thickness also relates to the distance corresponding to maximum misfit. In general, travel time anomalies are the largest for deeper diving waves owing to longer path lengths inside the LLSVP. The best-fitting model (see green lines in Fig. 6e and 6f) is a 600 km thick LLSVP with a constant 1.5% shear velocity reduction, and the LLSVP top distributed over 100 km (Fig. 6g). The broadened waveforms are visible in single records, but also in stacked data for the shaded region of Fig. 6a (Fig. S8, Supplementary Material). While we expect the shear velocity structure inside the LLSVP to be variable (due to variable temperature and possibly composition), the 1D model approximates the general trend of the data reasonably well.

The travel times are under-predicted for the deeper diving waves; this is not unexpected: we explored constant velocity reduction LLSVPs in the 1-D modeling with emphasis on the waveform effects of the LLSVP top. Approaching the CMB, the shear velocities have been shown to reduce significantly (Ritsema et al., 1997; Bréger and Romanowicz, 1998). Assuming constant seismic properties within the LLSVP can bias predictions of seismic ray path, and hence bias the imaged shape of LLSVPs, particularly for studies that rely on travel times to map the shape. Event mislocations can also affect travel time studies. Here, we preferentially map the shape with pulse-broadening information, and do not expect strong dependency upon reference model (Fig. S9, Supplementary Material). Also, obviously, there are shortcomings to 1D travel time modeling in a region of the mantle where we know strong 3D variations exist. Our intent in the model exploration for travel times was to gain a basic understanding of bulk travel time trends for a significant velocity reduction (i.e., the LLSVP top) at some lower mantle depth, and to see if it is consistent with waveform broadening inference for LLSVP top, which is indeed suggested here.

The large misfits near 600 km above the CMB in the cross-section of Fig. 6a are therefore consistent with the top of the LLSVP in the 1-D model; strong misfits above this depth may correspond to a morphological ridge of the compositional reservoir – a feature seen in the geodynamic modeling and argued for in the African LLSVP (Sun et al., 2010). Although less strong and sharp than that used in modeling of the African LLSVP (e.g. −3% over 50 km; Ni et al., 2002), our imaged reduction is nearly twice that inferred from double-array stacking in our study region (Lay et al., 2006). Some waveform misfits outside of the highlighted azimuthal sector are larger, consistent with a greater sharpness to the LLSVP top, and/or a greater drop in LLSVP velocities there (i.e., a greater velocity contrast at the LLSVP edge). In this paper the seismic analyses and modeling focus on the general data trends. Future work will require a more complete assessment of 2- and 3-D affects from the imaged LLSVP morphologies.

6. Discussion

As discussed, sharp sides of LLSVPs have been advocated by a number of seismic studies (Fig. 1). This study focuses on the sloped side and sharp top to the Pacific LLSVP beneath Hawaii. It is important to compare and contrast to the African LLSVP. Several studies (Table S1) have invoked a sharp top for the African LLSVP; most recently, careful travel time and waveform analyses by Sun and Miller (2013) demonstrate a sharp top on the western edge of the African LLSVP. This is consistent with our observations, and consistent with a distinct thermochemical origin to LLSVPs.

Mantle plumes are hypothesized to sample material distinct from the upper mantle sources of MORBs. Some plumes bring recycled crustal components back to the surface while others supply material with chemical properties (particularly low ^{4}He/^{3}He ratios) expected for primitive mantle (Hofmann, 1997; Weis et al., 2011). The creation of new compositional heterogeneity and the preservation of ancient heterogeneity in the mantle depend upon the efficiency of the mixing accompanying mantle convection to homogenize chemically distinct material introduced into the mantle by plate subduction, or remaining from the initial differentiation of the Earth.

With the largest buoyancy flux of any intraplate hotspot on Earth (Sleep, 1990), the Hawaiian archipelago serves as an important test bed for various hypotheses regarding plume and source reservoir morphology, as well as mantle circulation and mixing. Seismic tomography supports Hawaii being the surface expression of a long-lived, deep-rooted mantle plume (Montelli et al., 2004; Wolfe et al., 2009), but incomplete data coverage results in blurring of actual structures (Ritsema et al., 2007), especially in the lowermost mantle. Waveform analyses have also long speculated that the CMB may be the source region of the Hawaiian plume (Russell et al., 1998; Thorne et al., 2004; Torsvik et al., 2010). One possibility is that plumes are associated with the margins of LLSVPs, rather than the central parts of LLSVPs (Thorne et al., 2004; Torsvik et al., 2010). The structure and dynamics of the mantle play an important role in governing plume morphology, from the plume root to the surface, but remain poorly constrained. Hawaii is situated above our LLSVP study region, and the distribution of misfits resembles a topographic peak of the LLSVP beneath Hawaii. Past tomographic models have low velocities that extend downwards beneath Hawaii to our triangular shaped LLSVP at the base of the mantle (Montelli et al., 2004; Wolfe et al., 2009), which is also apparent in larger scale global models (Mégnin and Romanowicz, 2000; Grand, 2002; Ritsema et al., 2011) (Fig. 7a).

The Hawaiian plume hypothesis is further supported by the upper mantle phase discontinuities at 410 and 660 km depth being perturbed in a manner consistent with elevated temperature (Schmerr et al., 2010) (Fig. 7b): the 410 discontinuity is deeper and the 660 discontinuity is shallower. We project the waveform misfit measurement of each record to the lowermost 50 km of the seismic ray path (e.g., the paths as in Fig. S3, Supplementary Material), and then volumetrically average them on a 3-D grid framework (Fig. 7c). We are unable to resolve structure above the 1980 km depth slice due to reduced data coverage (this would require sensors at smaller epicentral distances, but we are limited by the western edge of the North American continent – there are not sensors to the west of this). There is smoothing in the SW-to-NE direction due to lack of crossing ray paths. However, large waveform misfits are found near the tomographically inferred LLSVP margin, and as the LLSVP forms a peak above the CMB; the large misfits near this trend appear to slope upwards towards a peak located beneath the surface position of the Hawaiian hotspot (Fig. 7c). While there are uncertainties in the tomography as well as the mapped locations of the misfits, we note the peak also geographically coincides with the bottom of the tomographically imaged low-shear velocity conduit, consistent with a whole mantle plume originating from the topographic peak of the Pacific LLSVP.

The relative longevity of the Hawaiian hot spot (in the last ∼80–100 Myr) may be due to a relative stability in its feeding source – a plume rooted at the top of the Pacific LLSVP. The shape of the northeast portion of the Pacific LLSVP inferred from our waveform misfits is triangular in cross-section, comparable to the shape of long-lived dense compositionally-distinct thermochemical piles in numerical (Tackley, 2002; McNamara and Zhong, 2004, 2005) and laboratory (Jellinek and Manga, 2002) experiments, in which thermal plume upwellings are rooted at cusps along pile ridges (e.g., Fig. 6c). If the intrinsic density of the reservoir material is high enough for the piles to be long-lived at the CMB, material entrainment can occur at such ridge cusps (Jellinek and Manga, 2002; McNamara et al., 2010), and such entrained material may explain the trace element and iso-

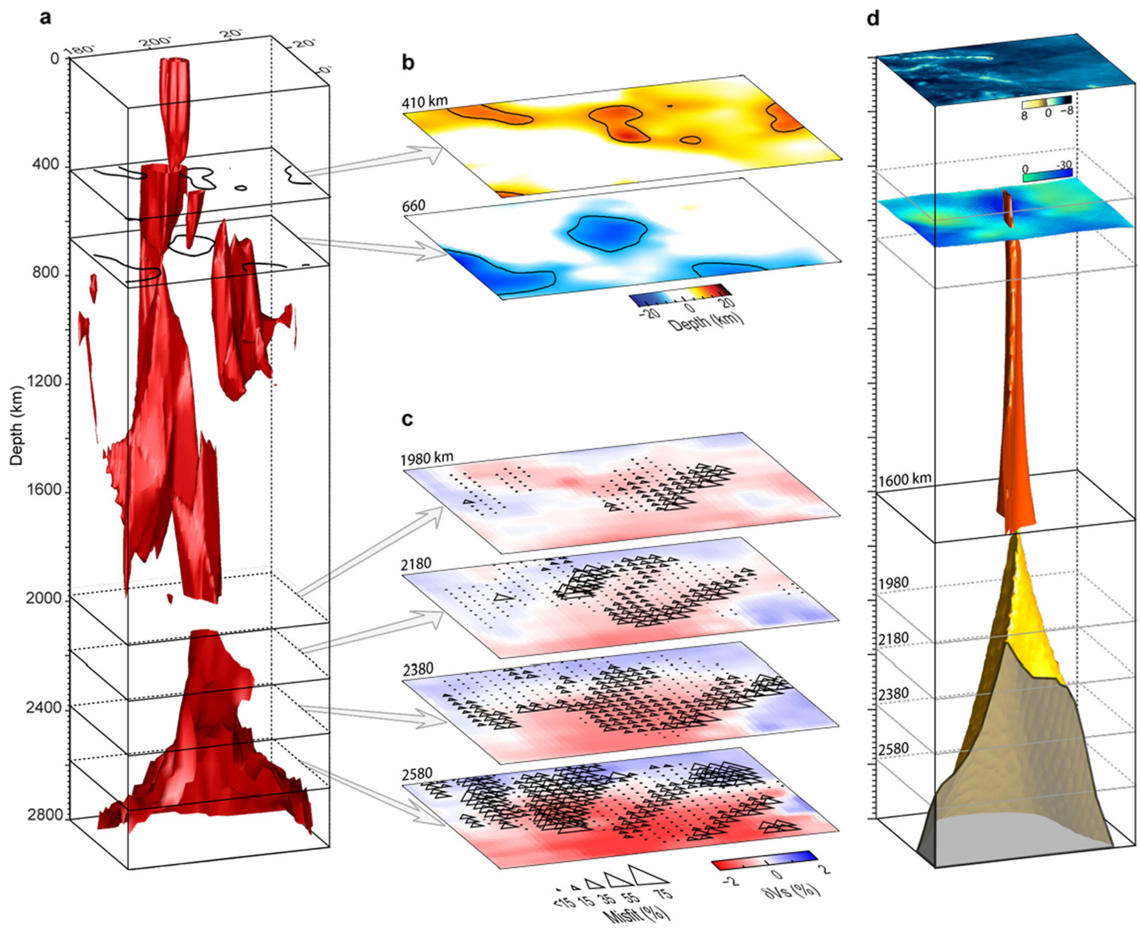

Fig. 7. Correlation of waveform misfits with tomography, transition zone thickness, geodynamic model. (a) 3D iso-surfaces of δVs tomography for 3 different models. From the surface to about 400 km, the iso-surface is at −1.5% for a regional tomography model (Wolfe et al., 2009). From about 400 km to 2000 km, the iso-surface is at −1.0% for another tomography model (Montelli et al., 2004). At 410 and 660 km depth, contours (black lines) for the transition zone discontinuity topography are also plotted (Schmerr et al., 2010). Below 2000 km, the iso-surface is at −0.9% for the global tomography model TXBW (Grand, 2002). Black boxes stand for the layer locations shown in the middle panel. (b) Discontinuity topography of 410 and 660, along with contours shown in (a). (c) Misfit values projected onto every point of the lowermost 50 km segments of PREM-predicted ray paths. Numbers denote the depth of each slice. We smoothed these path segments over a grid with spacing 2 by 2 degrees laterally, and 50 km in the depth direction. The smoothed misfit values (open triangles and black dots) are plotted on top of the shear-wave velocity perturbations of the tomography model TXBW. (d) The iso-surface of temperature (orange) for the upper 1600 km of the mantle, and iso-surface of composition (gold) for the rest of the mantle are shown. These iso-surfaces are based upon a geodynamically derived thermochemical convection model with a couple hundred kilometers thick dense layer at the bottom of the mantle (Garnero and McNamara, 2008). The map on the surface is the topography of the Hawaii region. Transition zone thickness estimates (Schmerr et al., 2010) are also shown as a surface plotted in between 410 and 660 km depth.

topic distinctions between Hawaiian lavas and MORB (Hart, 1984; Hofmann, 1997). If the entire reservoir is positively buoyant, the whole pile can rise up into the mantle as a superplume (Fig. 2c), which can similarly have sharp sides in the lowermost 1000 km of the mantle. Two important challenges remain for the superplume possibility: the morphology of the top of a superplume is predicted to be dome-shaped (Davaille, 1999), not a triangular ridged-top pile as seen here and in other geodynamic studies (Tackley, 2002; McNamara and Zhong, 2004, 2005; Jellinek and Manga, 2002). Secondly, if significant quantities of the LLSVP material are entrained into general mantle circulation, the imaged LLSVPs are either small remnants of originally much larger compositionally distinct reservoirs, or there must be a means to restock the LLSVP's if their volumes have not changed much over Earth history. Thus, unless the amount of LLSVP entrainment into the rising plume is small, which would require a large compositionally-induced density difference in the LLSVP material, the longevity of superplumes are likely limited, and it is unclear how many oscillations a superplume may undergo before being fully stirred into the background mantle.

Uncertainty in model parameters makes a direct comparison between geodynamical models and the actual Earth fraught with difficulty. However, to the first order, the strong chemical and thermal gradients at reservoir margins observed in the models (Fig. 6c) agree with patterns of broadened waveforms near the LLSVP edges observed here (also, see Fig. 1c). Models having dense material swept into piles (e.g., Fig. 2d) consistently display the hottest temperatures along the CMB immediately inside the piles at their boundary with the surrounding lower mantle. This is where flow from both within and outside the pile converges at the boundary, and these regions may be the most likely locations for ULVZs (Hernlund and Tackley, 2007; McNamara et al., 2010), small patches of material proposed to contain partial melt (McNamara et al., 2010). If ULVZs are more likely to be found beneath hotspots (Williams et al., 1998), then there may be a coupling between processes responsible for thermochemical pile margin morphology giving rise to plumes, and the hottest temperatures of basal mantle rock. ULVZs have been found near the LLSVP edge in our study region (e.g., McNamara et al., 2010; Cottaar and Romanowicz, 2012), consistent with inference from dynamics.

As mentioned earlier, our 1D velocity modeling is pursued to learn the general properties of velocity reductions with depth, in the context of a regional average, to compare to inferences from the waveform broadening analyses. More information is needed for stronger constraints on the 3D velocity variations within the LLSVP (notably, other phases and more data). S-wave travel times can also be affected by upper mantle heterogeneity and earthquake mislocations. Earthquake mislocations should not contribute to the general depth trends we see in travel times, but it is possible upper mantle structure might play a role. To explore this, we first plotted the tomography-model-corrected S travel time residuals versus depth in SOM Fig. S13; these can be compared to the uncorrected data in Fig. 6f. After correction, travel time residuals between 500 and 900 km above the CMB are closer to zero; residuals of deeper penetrating waves are reduced, but are still positive (Fig. S13a). The remaining left-over residual is consistent with past studies that assume the shape of the LLSVP from global tomography models, but increase the velocity reduction within the LLVSP (Ritsema et al., 1998; Wang and Wen, 2004; He and Wen, 2012), i.e., dVs reductions in LLSVP structure in tomography models is not strong enough. Thus, our bulk travel time trends are consistent with velocity decreasing in LLSVP structure in the lowermost 600 km or so of the mantle.

We have sought to model the position and the velocity drop of the top of the LLSVP. Both the travel time increase with depth between 400–700 km above the CMB (Fig. 6f) and misfit peak at around 600 km above the CMB (Fig. 6d) are the main trends we modeled. However, it is possible that the upper mantle plays a role in broadening waveforms. To explore this we project the S misfits to beneath the stations and plot them with upper mantle shear velocity variations in tomography models at various depths (Supplementary Online Fig. S14). A geographic correlation between waveform broadening and patterns in upper mantle heterogeneity is not clear, especially in comparison to the correlation pattern with LLSVP margins. Combined with the SS lacking the broadening seen in S (Fig. S13), the evidence points to a lower mantle source for the large misfit values measured and analyzed here.

Mantle attenuation can contribute to pulse broadening. For example, variable attenuation across the North American upper mantle explains waveform variability across EarthScope's Transportable Array (Lawrence et al., 2006). In that study, the strongest attenuation is in the western most US. Thus upper mantle attenuation may contribute to some waveform deviations in our dataset recorded there. However, strong waveform broadening in our data set is seen in the central US (e.g., Fig. S14), where upper mantle attenuation in Lawrence et al. (2006) is weak (though, their station coverage is poor there).

Here we explore how attenuation in the deeper mantle might contribute to waveform broadening. We test increased attenuation (hence, low quality factor, Q, which is inversely proportional to attenuation) in the lowest 600 km of the mantle, a depth shell thickness chosen to correspond to our preferred LLSVP thickness for the azimuth we modeled in Fig. 6. We computed reflectivity synthetic seismograms for the shear Q values of 312 (PREM), 200, 100, 50, and 25, for that 600 km lowermost mantle shell. To isolate the contribution from attenuation, we kept the velocity structure to be that of PREM. Misfit values were computed for these traces relative to synthetics for PREM's Q, as well as differential t^* operator values to best correlate the PREM synthetics to the high attenuation (low Q) models. These are shown in Supplementary Figs. S15 and S16. Fig. S15 displays synthetic waveforms, differential t^* values, and cross-correlation coefficients. Fig. S16 shows the misfit for a range of differential t^* values. These synthetic experiments show that very low Q (e.g., model Q05, where $Q = 25$) significantly broadens the deeper diving S wave at 90 degrees. The shallower S wave at 80 degrees is also broadened with a misfit close to 50% for this extreme model, but not as much as the deeper diving S. Perhaps low Q deep in the LLSVP can contribute to the broadened deeper diving S waves we see (but don't model, e.g., Fig. 6a–d), but our approach does not constrain the degree to which multiple paths (e.g., Fig. 5) versus attenuation (Fig. S15) contribute to these data. It is for this reason we have limited our analyses to the more shallow diving waves. It is also noteworthy that the cross-correlation coefficients diminish for the lowest Q models (Fig. S15), which might help to constrain Q versus structure for the deeper diving waves in future work.

7. Conclusions

We developed a new method to systematically quantify the distortion of S waveforms sampling the northeast portion of the Pacific LLSVP. We show that data with waveform broadening sample the LLSVP's margins where there are strong velocity gradients along its sides and top, extending some 600–900 km up off the CMB into the overlying mantle. The pattern or broadened waveforms suggest the LLSVP top forms a topographical peak. Spatial correlation between the location of the peak, topography of transition zone discontinuities, and the Hawaiian islands supports the hypothesis that a nearly vertical mantle plume beneath Hawaii may originate from the LLSVP topographic peak. The sloped side of the LLSVP provides evidence that it is a long-lived thermochemical pile. Thermal gradients along the pile edges can foster plumes that can entrain long-lived deep mantle reservoir material leading to isotopic and chemical signatures unique to hotspot basalts.

Acknowledgements

This research was funded in part by awards from the National Science Foundation (NSF) EAR0948591 and EAR1161038. The detailed reviews of 5 anonymous reviewers significantly helped to improve the manuscript. We are especially grateful to the Incorporated Research Institutions for Seismology (IRIS) for making the seismic data freely available, and NSF's EarthScope program that made the high density seismic network possible, without which this work would not have been possible.

Appendix A. Supplementary material

Supplementary material related to this article can be found online at http://dx.doi.org/10.1016/j.epsl.2015.06.012.

References

Becker, T.W., Boschi, L., 2002. A comparison of tomographic and geodynamic mantle models. Geochem. Geophys. Geosyst. 3 (1), 1003. http://dx.doi.org/10.1029/2001GC000168.

Brandenburg, J.P., van Keken, P.E., 2007. Deep storage of oceanic crust in a vigorously convecting mantle. J. Geophys. Res. 112. http://dx.doi.org/10.1029/2006jb004813.

Bréger, L., Romanowicz, B., 1998. Three-dimensional structure at the base of the mantle beneath the central Pacific. Science 282, 718–720. http://dx.doi.org/10.1126/science.282.5389.718.

Bull, A.L., McNamara, A.K., Ritsema, J., 2009. Synthetic tomography of plume clusters and thermochemical piles. Earth Planet. Sci. Lett. 278, 152–162. http://dx.doi.org/10.1016/j.epsl.2008.11.018.

Christensen, U.R., Hofmann, A.W., 1994. Segregation of subducted oceanic crust in the convecting mantle. J. Geophys. Res. 99, 19867–19884. http://dx.doi.org/10.1029/93JB03403.

Cottaar, S., Romanowicz, B., 2012. An unusually large ULVZ at the base of the mantle near Hawaii. Earth Planet. Sci. Lett. 355–356, 213–222. http://dx.doi.org/10.1016/j.epsl.2012.09.005.

Davaille, A., 1999. Simultaneous generation of hotspots and superswells by convection in a heterogeneous planetary mantle. Nature 402, 756–760. http://dx.doi.org/10.1038/45461.

Davies, D.R., Goes, S., Schuberth, B.S.A., Bunge, H.P., Ritsema, J., 2012. Reconciling dynamic and seismic models of Earth's lower mantle: the dominant role of thermal heterogeneity. Earth Planet. Sci. Lett. 353, 253–269. http://dx.doi.org/10.1016/j.epsl.2012.08.016.

Dziewonski, A.M., Anderson, D.L., 1981. Preliminary reference earth model (PREM). Phys. Earth Planet. Inter. 25, 297–356. http://dx.doi.org/10.1016/0031-9201(81)90046-7.

Ford, S.R., Garnero, E.J., McNamara, A.K., 2006. A strong lateral shear velocity gradient and anisotropy heterogeneity in the lowermost mantle beneath the southern Pacific. J. Geophys. Res. 111, 1–14. http://dx.doi.org/10.1029/2004JB003574.

Garnero, E.J., McNamara, A.K., 2008. Structure and dynamics of Earth's lower mantle. Science 320, 626–628. http://dx.doi.org/10.1126/science.1148028.

Grand, S.P., 2002. Mantle shear-wave tomography and the fate of subducted slabs. Philos. Trans. R. Soc. Lond. 360, 2475–2491. http://dx.doi.org/10.1098/rsta.2002.1077.

Hart, S.R., 1984. A large-scale isotope anomaly in the Southern Hemisphere mantle. Nature 309, 753–757. http://dx.doi.org/10.1038/309753a0.

He, Y., Wen, L., 2009. Structural features and shear-velocity structure of the "Pacific Anomaly". J. Geophys. Res. 114, B02309. http://dx.doi.org/10.1029/2008JB005814.

He, Y., Wen, L., 2012. Geographic boundary of the "Pacific Anomaly" and its geometry and transitional structure in the north. J. Geophys. Res. 117, B09308. http://dx.doi.org/10.1029/2012JB009436.

Hernlund, J.W., Tackley, P.J., 2007. Some dynamical consequences of partial melting in Earth's deep mantle. Phys. Earth Planet. Inter. 162, 149–163. http://dx.doi.org/10.1016/j.pepi.2007.04.005.

Hofmann, A.W., 1997. Mantle geochemistry: the message from oceanic volcanism. Nature 385, 219–229. http://dx.doi.org/10.1038/385219a0.

Houser, C., Masters, G., Shearer, P., Laske, G., 2008. Shear and compressional velocity models of the mantle from cluster analysis of long-period waveforms. Geophys. J. Int. 174 (1), 195–212. http://dx.doi.org/10.1111/j.1365-246X.2008.03763.x.

Ishii, M., Tromp, J., 1999. Normal-mode and free-air gravity constraints on lateral variations in velocity and density of Earth's mantle. Science 285, 1231–1236. http://dx.doi.org/10.1126/science.285.5431.1231.

Jellinek, A.M., Manga, M., 2002. The influence of a chemical boundary layer on the fixity, spacing and lifetime of mantle plumes. Nature 418, 760–763. http://dx.doi.org/10.1038/nature00898.1.

Lawrence, J.F., Shearer, P.M., Masters, G., 2006. Mapping attenuation beneath North America using waveform cross-correlation and cluster analysis. Geophys. Res. Lett. 33, L07315.

Lay, T., Hernlund, J., Garnero, E.J., Thorne, M.S., 2006. A post-perovskite lens and D″ heat flux beneath the central Pacific. Science 314, 1272–1276. http://dx.doi.org/10.1126/science.1133280.

Lekic, V., Cottaar, S., Dziewonski, A., Romanowicz, B., 2012. Cluster analysis of global lower mantle tomography: a new class of structure and implications for chemical heterogeneity. Earth Planet. Sci. Lett. 357–358, 68–77. http://dx.doi.org/10.1016/j.epsl.2012.09.014.

Luo, S., Ni, S., Helmberger, D.V., 2001. Evidence for a sharp lateral variation of velocity at the core–mantle boundary from multipathed PKPab. Earth Planet. Sci. Lett. 189, 155–164. http://dx.doi.org/10.1016/S0012-821X(01)00364-8.

Manga, M., Jeanloz, R., 1996. Implications of a metal-bearing chemical boundary layer in D″ for mantle dynamics. Geophys. Res. Lett. 23, 3091–3094. http://dx.doi.org/10.1029/96GL03021.

Masters, G., Laske, G., Bolton, H., Dziewonski, A.M., 2000. The relative behavior of shear velocity, bulk sound speed, and compressional velocity in the mantle: implications for chemical and thermal structure. In: Karato, S., Forte, A.M., Liebermann, R.C., Masters, G., Stixrude, L. (Eds.), Earth's Deep Interior, vol. 117. American Geophysical Union, Washington, DC, pp. 63–87.

McNamara, A.K., Zhong, S., 2004. Thermochemical structures within a spherical mantle: superplumes or Piles? J. Geophys. Res. 109, B07402. http://dx.doi.org/10.1029/2003JB002847.

McNamara, A.K., Zhong, S., 2005. Thermochemical structures beneath Africa and the Pacific Ocean. Nature 437, 1136–1139. http://dx.doi.org/10.1038/nature04066.

McNamara, A.K., Garnero, E.J., Rost, S., 2010. Tracking deep mantle reservoirs with ultra-low velocity zones. Earth Planet. Sci. Lett. 299, 1–9. http://dx.doi.org/10.1016/j.epsl.2010.07.042.

Mégnin, C., Romanowicz, B., 2000. The shear velocity structure of the mantle from the inversion of body, surface, and higher modes waveforms. Geophys. J. Int. 143, 709–728. http://dx.doi.org/10.1046/j.1365-246X.2000.00298.x.

Montelli, R., Nolet, G., Dahlen, F.A., Masters, G., Engdahl, E.R., Hung, S.H., 2004. Finite-frequency tomography reveals a variety of plumes in the mantle. Science 303, 338–343. http://dx.doi.org/10.1126/science.1092485.

Müller, G., 1985. The reflectivity method—a tutorial. J. Geophys. 58, 153–174.

Ni, S., Tan, E., Gurnis, M., Helmberger, D.V., 2002. Sharp sides to the African superplume. Science 296, 1850–1852. http://dx.doi.org/10.1126/science.1070698.

Rawlinson, N., Kennett, B.L.N., 2004. Rapid estimation of relative and absolute delay times across a network by adaptive stacking. Geophys. J. Int. 157, 332–340. http://dx.doi.org/10.1111/j.1365-246X.2004.02188.x.

Ritsema, J., Garnero, E.J., Lay, T., 1997. A strongly negative shear velocity gradient and lateral variability in the lowermost mantle beneath the Pacific. J. Geophys. Res. 102, 20395–20411. http://dx.doi.org/10.1029/97JB01507.

Ritsema, J., Ni, S., Helmberger, D.V., 1998. Evidence for strong shear velocity reductions and velocity gradients in the lower mantle beneath Africa. Geophys. Res. Lett. 25, 4245–4248. http://dx.doi.org/10.1029/1998GL900127.

Ritsema, J., McNamara, A.K., Bull, A.L., 2007. Tomographic filtering of geodynamic models: implications for model interpretation and large-scale mantle structure. J. Geophys. Res. 112, B01303. http://dx.doi.org/10.1029/2006JB004566.

Ritsema, Deuss A, J., van Heijst, H.J., Woodhouse, J.H., 2011. S40RTS: a degree-40 shear-velocity model for the mantle from new Rayleigh wave dispersion, teleseismic traveltime and normal-mode splitting function measurements. Geophys. J. Int. 184, 1223–1236. http://dx.doi.org/10.1111/j.1365-246X.2010.04884.x.

Rost, S., Earle, P., 2010. Identifying regions of strong scattering at the core–mantle boundary from analysis of PKKP precursor energy. Earth Planet. Sci. Lett. 297, 616–626. http://dx.doi.org/10.1016/j.epsl.2010.07.014.

Russell, S., Lay, T., Garnero, E.J., 1998. Seismic evidence for small-scale dynamics in the lowermost mantle at the root of the Hawaiian hotspot. Nature 369, 255–257. http://dx.doi.org/10.1038/24364.

Schmerr, N., Garnero, E.J., McNamara, A.K., 2010. Deep mantle plumes and convective upwelling beneath the Pacific Ocean. Earth Planet. Sci. Lett. 294, 143–151. http://dx.doi.org/10.1016/j.epsl.2010.03.014.

Schubert, G., Masters, G., Olson, P., Tackley, P., 2004. Superplumes or plume clusters? Phys. Earth Planet. Inter. 146, 147–162. http://dx.doi.org/10.1016/j.pepi.2003.09.025.

Schuberth, B.S.A., Bunge, H.P., Ritsema, J., 2009. Tomographic filtering of high-resolution mantle circulation models: can seismic heterogeneity be explained by temperature alone? Geochem. Geophys. Geosyst. 10. http://dx.doi.org/10.1029/2009gc002401.

Sleep, N.H., 1990. Hotspots and mantle plumes: some phenomenology. J. Geophys. Res. 95, 6715–6736. http://dx.doi.org/10.1029/JB095iB05p06715.

Sun, D., Miller, M.S., 2013. Study of the western edge of the African large low shear velocity province. Geochem. Geophys. Geosyst. 14, 3109–3125.

Sun, D., Tan, E., Helmberger, D.V., Gurnis, M., 2007. Seismological support for the metastable superplume model, sharp features, and phase changes within the lower mantle. Proc. Natl. Acad. Sci. 104, 9151–9155. http://dx.doi.org/10.1073/pnas.0608160104.

Sun, D., Helmberger, D., Gurnis, M., 2010. A narrow mid-mantle plume below southern Africa. Geophys. Res. Lett. 37, L09302. http://dx.doi.org/10.1029/2009GL042339. 5 pp.

Tackley, P.J., 2002. Strong heterogeneity caused by deep mantle layering. Geochem. Geophys. Geosyst. 3. http://dx.doi.org/10.1029/2001GC000167.

Tackley, P.J., 2012. Dynamics and evolution of the deep mantle resulting from thermal, chemical, phase and melting effects. Earth-Sci. Rev. 110, 1–25. http://dx.doi.org/10.1016/j.earscirev.2011.10.001.

Tackley, P.J., Xie, S., Nakagawa, T., Hernlund, J.W., 2005. Numerical and laboratory studies of mantle convection: philosophy, accomplishments and thermochemical structure and evolution. In: Earth's Deep Mantle: Structure, Composition, and Evolution. In: Geophysical Monograph Series, vol. 160, pp. 83–99. http://dx.doi.org/10.1029/160GM07.

Tan, E., Gurnis, M., 2005. Metastable superplumes and mantle compressibility. Geophys. Res. Lett. 32, L20307. http://dx.doi.org/10.1029/2005GL024190.

Tan, E., Leng, W., Zhong, S., Gurnis, M., 2011. On the location and mobility of thermo-chemical structures with high bulk modulus in the 3-D compressible mantle. Geochem. Geophys. Geosyst. 12. http://dx.doi.org/10.1029/2011GC003665.

Thorne, M., Garnero, E.J., Grand, S.P., 2004. Geographic correlation between hot spots and deep mantle lateral shear-wave velocity gradients. Phys. Earth Planet. Inter. 146, 47–63. http://dx.doi.org/10.1016/j.pepi.2003.09.026.

To, A., Romanowicz, B., Capdeville, Y., Takeuchi, N., 2005. 3D effects of sharp boundaries at the borders of the African and Pacific Superplumes: observation and modeling. Earth Planet. Sci. Lett. 233, 137–153. http://dx.doi.org/10.1016/j.epsl.2005.01.037.

Torsvik, T.H., Burke, K., Steinberger, B., Webb, S.J., Ashwal, L.D., 2010. Diamonds sampled by plumes from the core–mantle boundary. Nature 466, 352–355. http://dx.doi.org/10.1038/nature09216.

Trampert, J., Deschamps, F., Resovsky, J., Yuen, D., 2004. Probabilistic tomography maps chemical heterogeneities throughout the lower mantle. Science 306, 853–856. http://dx.doi.org/10.1126/science.1101996.

Wang, Y., Wen, L., 2004. Mapping the geometry and geographic distribution of a very-low velocity province at the base of the Earth's mantle. J. Geophys. Res. 109, B10305. http://dx.doi.org/10.1029/2003JB002674.

Weis, D., Garcia, M.O., Rhodes, J.M., Jellinek, M., Scoates, J.S., 2011. Role of the deep mantle in generating the compositional asymmetry of the Hawaiian mantle plume. Nat. Geosci. 4, 831–838. http://dx.doi.org/10.1038/NGEO1328.

Wen, L., 2001. Seismic evidence for a rapidly-varying compositional anomaly at the base of the Earth's mantle beneath the Indian Ocean. Earth Planet. Sci. Lett. 194, 83–95. http://dx.doi.org/10.1016/S0012-821X(01)00550-7.

Williams, Q., Revenaugh, J., Garnero, E., 1998. A correlation between ultra-low basal velocities in the mantle and hot spots. Science 281, 546–549. http://dx.doi.org/10.1126/science.281.5376.546.

Wolfe, C.J., Solomon, S.C., Laske, G., Collins, J.A., Detrick, R.S., Orcutt, J.A., Bercovici, D., Hauri, E.H., 2009. Mantle shear-wave velocity structure beneath the Hawaiian hot spot. Science 326, 1338–1390. http://dx.doi.org/10.1126/science.1180165.